Ion Velocimetry Measurements and Particle-In-Cell Simulation of a Cylindrical Cusped Plasma Accelerator

IEPC-2013-458

Presented at the 33^{rd} International Electric Propulsion Conference,
The George Washington University, Washington, D.C., USA
October 6–10, 2013

A. Lucca Fabris[1*], C. V. Young[2†], M. Manente[1‡], D. Pavarin[1§], and M. A. Cappelli[2¶]
1) University of Padova, Padova, 35131, Italy
2) Stanford University, Stanford, CA 94305, USA

The Stanford Cylindrical Cusped Field Thruster (CCFT) has been investigated experimentally and numerically with particular focus on the exit plane acceleration region near the top magnetic cusp. Time-averaged xenon ion laser induced fluorencence measurements using the $5d[4]_{7/2} - 6p[3]_{5/2}$ ($\lambda = 843.72$ nm) Xe II transition have mapped the total ion velocity vectors in this region. The thruster is also simulated using the fully kinetic 3D particle-in-cell code F3MPIC. The consistent experimental and numerical results give physical insight into the mechanisms of ion acceleration and the role of the magnetic field topology in determining ion trajectories and plume divergence. The electrons are strongly magnetized and follow the magnetic field structure, grouping near the cusps. A steep potential drop over a few millimeters near the exit plane tracks the magnetic separatrix of the top cusp and is consistent with measured ion velocity vectors. A characteristic conical region of high ion density, peak ion velocity, and visible emission is observed in the experimental and simulated plume, with an estimated divergence half angle of $30°$.

Nomenclature

CCFT	= Cylindrical Cusped Field Thruster
CHT	= Cylindrical Hall Thruster
DCFT	= Divergent Cusped Field Thruster
LIF	= Laser Induced Fluorescence
IVDF	= Ion Velocity Distribution Function
OG	= Optogalvanic
PIC	= Particle-in-Cell
PMT	= Photomultiplier Tube
c	= Speed of light (2.98×10^8 m/s)
h	= Planck's constant (6.626×10^{-34} m$^2\cdot$ kg/s)
I_{sp}	= Specific Impulse (s)
M_i	= Xenon ion mass (131.29 amu)
q	= Singly ionized xenon charge (1.602×10^{-34} C)
R	= Radial position coordinate (mm)
v	= Ion velocity component parallel to exciting laser in LIF (m/s)
v_{ax}	= Axial measured ion velocity component (m/s)

*Ph.D. Candidate, Center of Studies and Activities for Space, andrea.luccafabris@gmail.com
†Ph.D. Candidate, Mechanical Engineering Department, cvyoung@stanford.edu
‡Postdoctoral Research Fellow, Center of Studies and Activities for Space, m.manente@gmail.com
§Researcher, Mechanical Engineering Department, Center of Studies and Activities for Space, daniele.pavarin@unipd.it
¶Professor, Mechanical Engineering Department, cap@stanford.edu

v_r = Radial calculated ion velocity component (m/s)
v_{30} = 30° off-axis measured ion velocity component (m/s)
Z = Axial position coordinate (mm)
ΔE_{12} = Energy gap of LIF absorption transition (J)
ΔE_{23} = Energy gap of LIF fluorescence transition (J)
Δv = Ion velocity increase due to potential drop (m/s)
Δx = PIC mesh size (mm)
$\Delta \phi$ = Potential drop (V)
λ = Wavelength (nm)
λ_D = Doppler correction to wavelength (nm)
λ_{De} = Debye length (mm)
λ_{ex} = Exciting laser wavelength absorbed by a moving ion (nm)
λ_{12} = Wavelength of LIF absorption transition (nm)
λ_{23} = Wavelength of LIF fluorescence transition (nm)
θ = Ion velocity vector direction, measured from thruster axis (rad)

I. Introduction

Recent attention given to small, low cost space vehicles has created a need for efficient, low power propulsion technology. Hall thrusters are capable of servicing this low power regime; however, several issues arise when scaling existing models down in power. Increased heat flux to the discharge channel walls, especially the center pole piece in annular Hall thrusters, erodes insulation more quickly and limits the lifetime of the device.[1,2] Increased ion sputtering to the channel walls has also been shown to reduce the usable life of the thruster.[3] Additionally, it is not well understood how cross-field transport mechanisms, which restrict electron flow to the anode, scale when decreasing thruster size and power requirements.

Several novel designs address these issues inherent with scaled down Hall thrusters, including the Cylindrical Hall Thruster (CHT, Princeton),[4] Diverging Cusped Field Thruster (DCFT, MIT)[5] and the Cylindrical Cusped Field Thruster (CCFT, Stanford).[6] The CHT design mitigates heat loading and erosion by retracting the overloaded center pole piece and pushing the ion acceleration region largely outside the discharge channel.[7–9] The CHT has demonstrated $\sim 25\%$ anode effeciencies when operating with xenon between 100 and 200 W.[10] The DCFT has a conical discharge channel with three permanent magnetic cusps that diminish in strength towards the exit plane. Magnetic bottles between cusps increase electron residence time, creating efficient ionization regions; mitigate electron flow directly to the anode; and minimize wall interactions through the mostly axial magnetic field.[11] The DCFT has demonstrated around 40% anode efficiency at 200 W.[5]

This paper presents an experimental and computational study of the CCFT operating on xenon. The cylindrical variant employs a cusped permanent magnetic field profile that weakens towards the exit plane to qualitatively reproduce the diverging DCFT magnetic profile. Previous CCFT studies with krypton demonstrated anode efficiencies of around 23% when operated between 40 to 240 W.[6] This work extends a recent study[12] of the CCFT operating with the more commonly used xenon propellant in which axial ion velocity components in the very near field of the discharge were measured with the nonintrusive laser induced fluorescence (LIF) method. We fully determine the ion velocity vector field near the exit plane on a denser measurement grid with two LIF traces at each point: one with the incident beam parallel to the main thruster axis and one with the thruster rotated by 30°. The commonly used Xe II (ion) $5d[4]_{7/2} - 6p[3]_{5/2}$ transition at 843.72 nm (air) is probed to determine the most probable time-averaged ion velocity in the measurement volume, while an optogalvanic (OG) trace of the Xe I (neutral) $6s'[1/2]_1 - 6p'[3/2]_2$ transition at 834.68 nm (air) in a hollow cathode lamp provides the stationary reference. The acquired velocity field is then compared with previous potential measurements[12] obtained with a floating emissive probe and the thruster magnetic profile simulated by finite element method magnetics (FEMM),[13] yielding physical insight into how these various aspects of the thruster combine to influence its overall operation.

We also simulate the CCFT using the the fully kinetic 3D Particle-In-Cell (PIC) code F3MPIC,[14] developed at the University of Padova, to validate and extend the experimental measurements. The PIC method[15] is a common approach for simulating a broad range of plasma phenomena, including plasma propulsion systems.[16–18] These codes are frequently based on a hybrid method in which ions are treated kinetically in a surrounding electron fluid, removing the need to resolve the system at the much faster time scale of electron motion. In the simulations presented here, both ions and electrons are treated as particles. Developed originally for plasma propulsion applications, F3MPIC has also been successfully applied to other plasma systems such as ion sources for the selective production of exotic species.[19] The exact CCFT geometry and magnetic field profile is mapped to a 3D tetrahedral mesh to study the magnetized particle dynamics present in the real device. The experimental anode and cathode potentials are imposed as boundary conditions for the finite element electrostatic solver. Simulation results are presented and compared with the experimental ion velocity and plasma potential measurements.

II. Stanford Cylindrical Cusped Field Thruster (CCFT)

The design and operating principles of the Stanford CCFT have been described in detail elsewhere[6,12,20] and are reviewed briefly here. A schematic of the Stanford CCFT appears in Fig. 1a, with the magnetic field profile simulated by finite element method magnetics (FEMM)[13] superimposed. The magnetic topology is generated by three samarium cobalt permanent magnets of alternating polarity that decrease in strength moving downstream away from the anode, separated by 1018 steel spacers to shape the field. This arrangement produces the diverging magnetic profile seen in the DCFT[5] even though the channel is cylindrical. The maximum magnetic field strength at the cusps is 0.45 T.

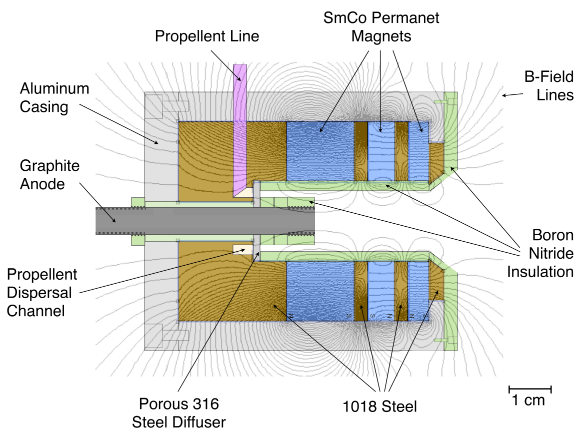

(a)

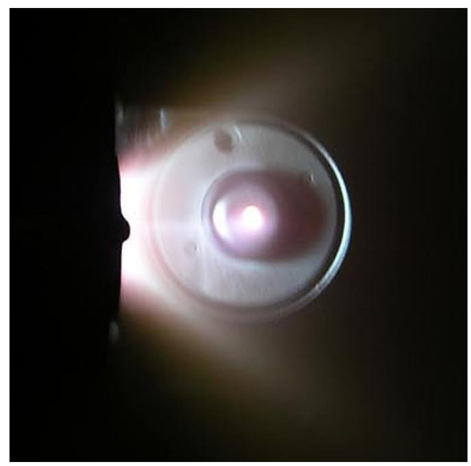

(b)

Figure 1: (a) Design schematic of the CCFT with magnetic topology superimposed, illustrating magnetic cusps of decreasing strength moving downstream from the anode. (b) The Stanford Cylindrical Cusped Field Thruster operating on xenon in the Stanford Plasma Physics Laboratory. The external cathode operating on argon is pictured behind the thruster, facing the camera.

Electrons are emitted by the external cathode (not pictured in Fig. 1a but seen in the background of Fig. 1b) and may either travel along magnetic field lines towards the thruster anode, biased at high positive potential relative to the grounded cathode body, or be ejected with the plume of ionized propellant atoms, neturalizing the discharge. Those electrons entering the discharge channel are impeded by the magnetic field structure, which is designed to trap electrons through magnetic mirroring between adjacent cusps and restrict electron flow to the graphite anode (located in a region of converging magnetic field). This resistance to electron migration establishes a primarily axial electric field that accelerates thrust-producing propellant ions away from the device. High energy electrons that overcome the sheath potential of the ceramic insulating wall and scatter may end up on magnetic field lines leading to an upstream cusp, or eventually to the anode. Regions between cusps with parallel magnetic field lines to the channel wall seek to reduce erosion by keeping particles away from the wall.

Xenon propellant is injected at the base of the channel through a porous steel diffuser. As propellant atoms encounter electrons with sufficient energy gained from the electric field, ionization events may occur. These secondary electrons may also become trapped in the magnetic cusps, increasing their residence time in the channel, and contribute to avalanche ionization. The resulting xenon ions are not affected by the magnetic field due to their high mass; however, the complicated interplay between the magnetic topology, ionization regions, and acceleration zones observed in the thruster may in fact produce an indirect link between the magnetic structure and eventual ion trajectories. Investigating this relationship further is a motivating factor for this work.

The thruster is encased in an aluminum cylinder 7 cm in length with a 6 cm outer diameter. The boron nitride cylindrical discharge channel is 1.4 cm in diameter and 4 cm in length up to the chamfered edge near the exit plane. This angled edge ensures that electrons traveling along magnetic field lines from the external cathode have a means of entering the channel without excessively impacting the front face of the thruster.[6] The anode is a partially threaded 0.64 cm diameter graphite rod.

The CCFT operating on xenon propellant is shown in Fig. 1a, where the conical plume of visible plasma (similar to that observed in the DCFT) suggests the beam angle is determined by the diverging magnetic field profile rather than the geometry of the channel. When operating previously on krypton, the CCFT demonstrated good performance in the 40-240 W range. With krypton flow rates of 5.9-8.9 sccm, the generated thrust is between 2-5 mN with specific impulse values up to 1200 s and total efficiencies up to 23%.[6]

III. Laser Induced Fluorescence Velocity Measurements

A. LIF Method

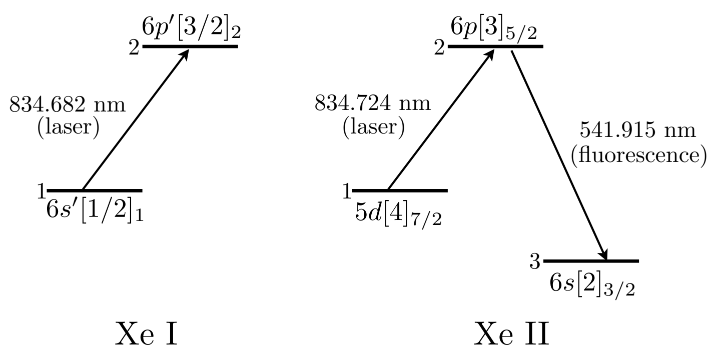

Figure 2: Xenon atomic transitions used in this work and the respective wavelengths in air. Xe I (neutrals) in a hollow cathode lamp are used as an optogalvanic stationary wavelength reference when probing moving Xe II (ions) in the thruster plume.

Laser induced fluorescence (LIF) velocimetry involves measuring a Doppler shift in the fluorescence excitation spectrum of a moving species as compared with a stationary reference. As pictured in Fig. 2, ions are pumped with a laser from an initial (usually metastable) state (1) to an excited upper state (2) that is shared by a second transition with strong fluorescence yield down to a third state (3). Ions absorb exciting photons of energy hc/λ_{12} equal to the energy level gap ΔE_{12} and consequently emit spontaneous fluorescence photons of energy hc/λ_{23} equal to the energy level gap ΔE_{23}, which are collected as the fluorescence signal. If an ion has a velocity component v in the same direction as the exciting laser, the incoming laser wavelength λ_{ex} is Doppler shifted (by an amount λ_D) in the ion frame; now the ion will only absorb an exciting photon whose energy with the Doppler correction is equal to the requisite hc/λ_{12} for the transition. This amounts to a change in the exciting laser wavelength λ_{ex} that is absorbed by the moving ion, as compared with λ_{12} that is absorbed by a stationary ion:

$$\lambda_{12} = \lambda_{ex} + \lambda_D = \lambda_{ex} + \frac{v}{c}\lambda_{ex} \tag{1}$$

$$\lambda_{ex} = \lambda_{12}\left(1 + \frac{v}{c}\right)^{-1}. \tag{2}$$

The same goes for the fluorescence process. The moving ion will still emit photons of wavelength λ_{23} in the ion frame, which translates to a Doppler shifted collected wavelength λ_{coll} of:

$$\lambda_{\text{coll}} = \lambda_{23} + \lambda_D = \lambda_{23}\left(1 + \frac{v}{c}\right) \tag{3}$$

in the laboratory frame. Since a distribution of ion velocities exists in the plasma, the exciting laser must be capable of scanning over a small wavelength range near the stationary value λ_{12} and the collection optics must pass fluorescence photons in a small bandwidth around the stationary value λ_{23}.

To obtain the Doppler shift used to back out ion velocities in the LIF measurement, first a laser wavelength scan is performed about a center value equal to λ_{12}. The emitted fluorescence is then collected through an optical system and a light sensor, typically a photomultiplier tube (PMT). A bandpass filter with a center wavelength λ_{23} is placed in the collection path in order to exclusively detect the fluoresced light originating from the target transition (2)-(3). When the scanning laser wavelength is equal to the effective excitation wavelength λ_{ex} for a given velocity class of ions, many ions are pumped to the excited state (2), producing a peak in the measured fluorescence intensity as the ions decay to state (3). Simultaneously in a stationary reference, ions with mean zero velocity produce a fluorescence peak as the laser scans through λ_{12}. Rearranging Eqn. (2) and using the measured peak wavelengths, the most probable ion velocity is then given as:

$$v = c\left(\frac{\lambda_{12}}{\lambda_{ex}} - 1\right). \tag{4}$$

The LIF diagnostic is reliable and by nature nonintrusive, avoiding perturbation of the surrounding plasma that can occur with probe-based techniques. Since the ionic transitions are narrow, LIF can nominally measure velocities at 100 m/s resolution. The measurement volume is defined by the intersection of the laser beam and collection optical path, allowing for fine spatial resolution. These advantages make LIF uniquely suited for characterizing the ejected plasma from a thruster or obtaining the local ion velocity distribution function in a plasma discharge. The most common implementation of LIF is time-averaged: the fluorescence photons are collected and integrated over a given time interval. However, time-synchronized measurements have also been conducted, locking the measurement into a specific phase of a periodic phenomena (e.g. the oscillating current mode observed in the DCFT).[21,22]

Figure 2 shows the two optical systems that are used in the determination of xenon ion velocities via LIF. The Xe I (neutral) $6s'[1/2]_1 - 6p'[3/2]_2$ transition at 834.682 nm is used in an optogalvanic (OG) reference measurement on a xenon hollow cathode lamp. Here, neutrals excited by the laser are more likely to become ionized and create free electrons in electron impact ionization events; the resulting extra electrons produce more free electrons in an avalanche ionization process, causing a temporary spike in the lamp's discharge current. The observed OG peak is then known to be located at $\lambda_{12} = 834.682$ nm during the laser scan. We utilize the Xe I line for the stationary reference because the much higher neutral xenon population in the lamp provides a stronger OG signal than the sparser xenon ion population. The Xe II (ion) $5d[4]_{7/2} - 6p[3]_{5/2}$ transition has been used previously for xenon ion velocity measurements in plasma thrusters[23–25] and the resulting fluorescence to the $6s[2]_{3/2}$ state at $\lambda_{23} = 541.915$ nm is collected for determining the Doppler shift in the absorbed laser radiation.

B. LIF Experimental Setup

A schematic of the LIF experimental setup in the Stanford Plasma Physics Laboratory (SPPL) is presented in Fig. 3. The exciting laser beam is generated by a New Focus TA-7600 semiconductor tapered amplifier which is seeded by a 20 mW tunable external-cavity diode laser (New Focus, Model TLB-6017) through a polarization-maintaining optical fiber. The maximum amplifier output power is 1 W; however, we limit the power to the $40 - 90$ mW range to avoid saturating the transition. The laser exhibits a mode hop free tuning range of 50 GHz (about 0.1 nm) and a linewidth narrower than 300 kHz. Wavelength modulation of the diode is obtained with a voltage ramp from a function generator (SRS Model DS345).

The beam emitted by the laser amplifier (lb1) passes through two beam samplers (BS1 and BS2) and enters a vacuum chamber window via a sequence of mirrors. The first beam sample (lb2, 10% of the main beam) is further separated into two minor beams (lb2a and lb2b) by means of a 50-50% beam splitter (BS3). Beam lb2a is directed to a Burleigh WA-1500 wavemeter for a rough wavelength measurement while tuning the laser parameters; we do not use the wavemeter for an exact determination of the laser wavelength during the scan as it is prone to inaccuracies and drift. The second minor beam (lb2b) is mechanically chopped (Chopper 2) and passes through a xenon hollow cathode lamp for a zero-velocity optogalvanic reference signal

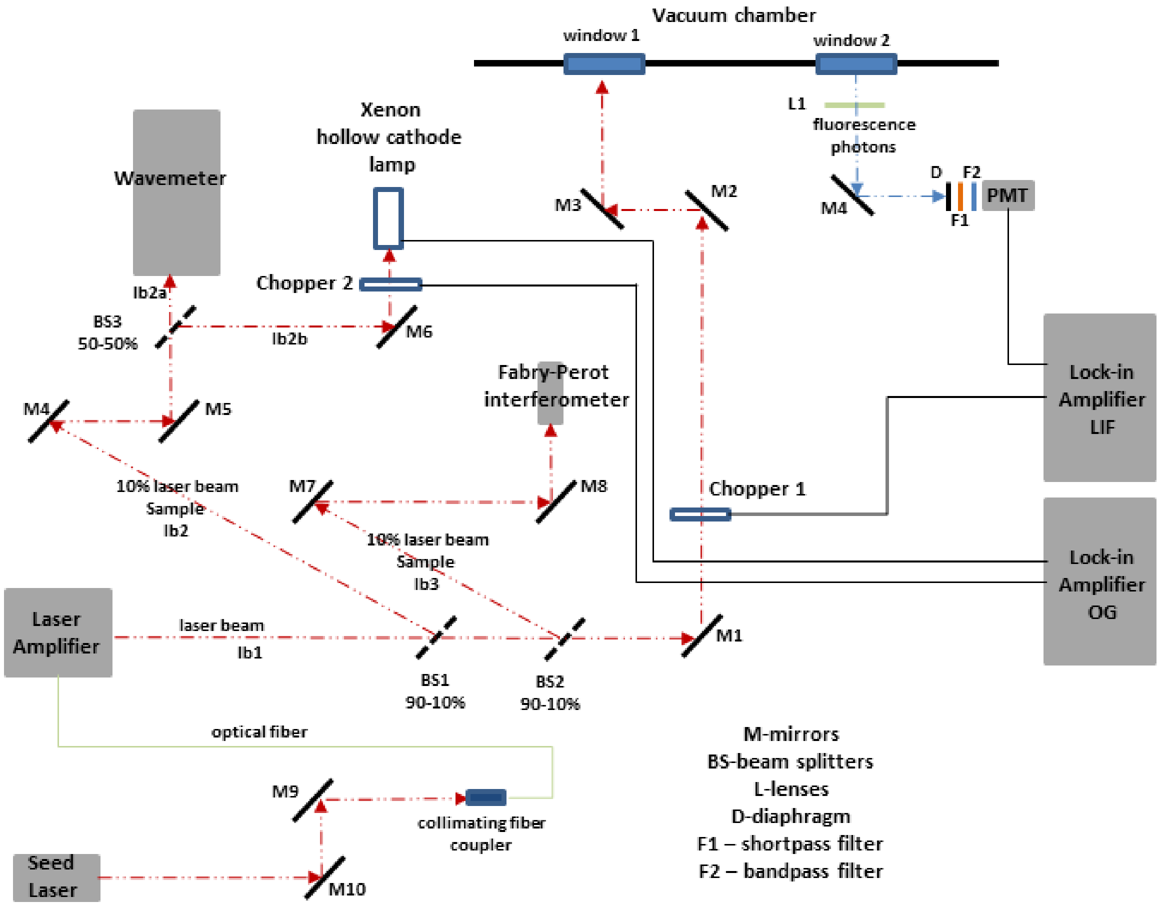

Figure 3: Schematic of laser induced fluorescence experimental setup.

(as described above). Perturbations in the lamp current due to the laser OG effect are detected through a 10 kΩ shunt resistor and a 700 nF capacitor to block the DC signal component. A lock-in amplifier then isolates the AC component at the chopping frequency. Another beam sample (lb3) is steered to a Fabry-Perot interferometer with a free spectral range of 1.5 GHz and a finesse of 200. The combined use of the Xenon hollow cathode lamp for the reference line and the Fabry-Perot interferometer allows a fine reconstruction of the wavelength as a function of time throughout the scan. Before entering the vacuum chamber, the main beam (lb1) is mechanically chopped (Chopper 1) at frequencies between 800 Hz and 2 kHz.

Once inside the chamber (Fig. 4), the beam is focused on the target plasma by a system of mirrors and lenses. Fluorescence photons are collected through a lens, directed back out of the chamber, and focused on the aperture of a photomultiplier tube (PMT) (Fig. 3). A 3 mm iris rejects background emission from the plasma outside of the target measurement volume to increase the signal to noise ratio. A shortpass filter with a 750 nm cutoff is used to reject any scattered laser light at 834-835 nm. Additionally, a 10 nm bandpass filter centered at 540 nm further restricts the collection system to detect only photons originating from the desired fluorescence transition at 541.92 nm. The collection system is aligned by firing a helium neon laser backwards through the collection path. The measurement volume is defined as the intersection between the main beam and the collection optical path (accounting for the iris), which is estimated to provide a spatial resolution of about 1 mm. Finally, the collected fluorescence signal from the PMT is processed by a second lock-in amplifier which extracts the signal component at the chopping frequency.

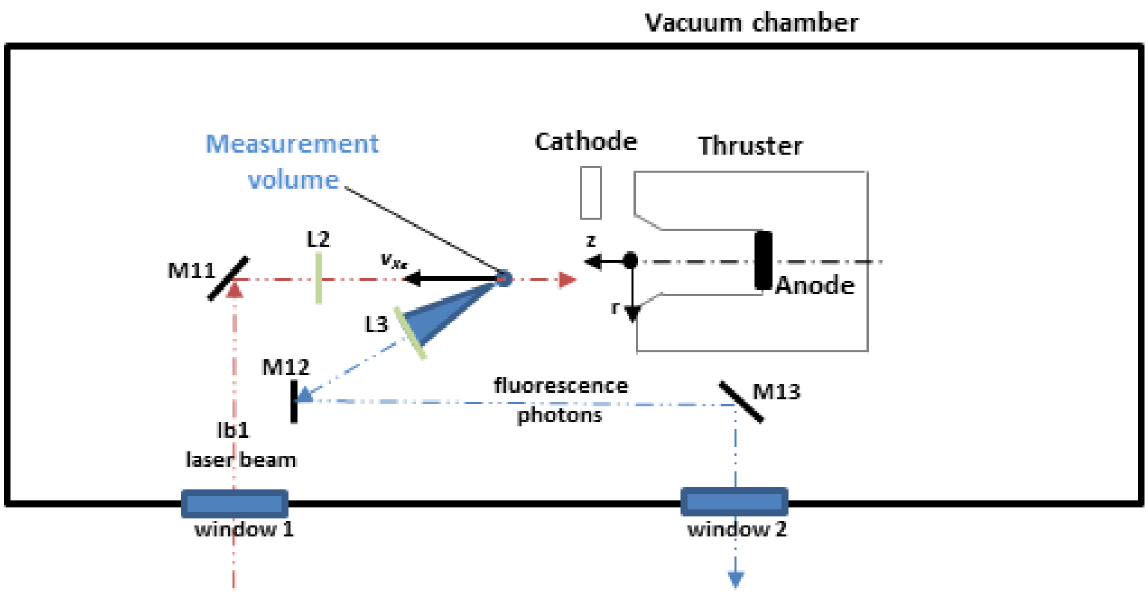

Figure 4: LIF experimental setup inside the vacuum chamber.

The SPPL high vacuum facility has been described previously in detail.[6] The stainless steel chamber is 4 m long and 1.25 m in diameter, equipped with a two-stage cryogenic cooling system. The first stage is two shrouds cooled with a Polycold Fast Cycle Water Vapor Cryopump (PFC, Model 1100), followed by two cryopanels cooled to 16 K with cryogenic helium. The pumping system provides an initial background pressure of 4×10^{-7} Torr and maintains a pressure of 2×10^{-5} Torr while operating the thruster.

The thruster is mounted on a two-axis horizontal motorized stage plus a 360° rotation stage for obtaining spatially resolved measurements – the LIF measurement volume remains fixed in space. A previous study[12] conducted axial LIF ion velocity measurements at several points near the CCFT exit plane in an 18 mm axial and 12 mm radial range. The current work extends these measurements to fully specify the velocity vectors, i.e. both magnitudes and directions, at a subset of points near the magnetic separatrix of the top cusp. This is accomplished through two LIF measurements at each point, one with the incident beam parallel to the thruster axis and one with the thruster rotated 30° off-axis. We choose 30° rather than a full 90° radial measurement based on geometrical constraints and the need to access inside the discharge channel. All data is taken on the cathode side of the plume, again for geometrical reasons.

To facilitate comparison with the previous axial LIF study,[12] the CCFT is operated in the same "power match" condition with a xenon mass flow rate of 586 μg/s and applied anode potential of 300 V, drawing ~0.4 A of current and 120 W of power from a Sorenson DCS-600-1.7 DC power supply. An IonTech (Model HCN-252) cathode is used as the electron source. The cathode, installed 28.3 mm downstream of the exit plane at a radius of 30 mm, is operated on argon propellant with a mass flow rate of 140 μg/s. The cathode keeper is operated in current limited mode at 0.25 A and the nominal heater current is 7 A.

C. LIF Results

Measured most probable ion velocities in the vicinity of the last CCFT cusp appear in Fig. 5. Recall that the most probable velocity is taken at the observed Doppler shifted peak in the Xe II fluorescence signal relative to the optogalvanic stationary Xe I reference; additional smaller peaks in the acquired signal may be indicative of multiple ion velocity classes present at the measurement location. Work to improve the LIF scans for extracting the entire spatially varying ion velocity distribution function (IVDF) is ongoing in the SPPL. Points where LIF traces are taken are indicated by Δ symbols. The acquired velocities are interpolated throughout the remainder of the domain using an inverse-distance method[12] where ϕ_s are the measured source point velocities and ϕ_d is the interpolated destination point velocity:

$$\phi_d = \frac{\sum w_s \phi_s}{\sum w_s} \tag{5}$$

$$w_s = D^{-E}. \tag{6}$$

The weighting function w_s is determined by the distance D between the source and destination points and a weighting factor E chosen here to be 3.5.[12] This value gives more weight to immediately adjacent source points and yields good smoothing. The white area in the lower right hand corner of the plots represents the angled thruster face near the exit plane ($Z = 0$, see Fig. 1a). Magnetic field lines calculated from FEMM[13] are indicated with dotted lines.

Figures 5a and 5b illustrate the measured velocity components with the exciting laser beam oriented parallel to the thruster axis ($R = 0$) and at a 30° counterclockwise rotation relative to the thruster axis, respectively. Inside the thruster discharge channel, the ions exhibit relatively slow axial velocities of about 2000 m/s. The axial acceleration begins to occur at $Z = -2$ mm, especially at radii close to the channel wall. Moving downstream, the axial acceleration front progressively penetrates towards the centerline. Figure 5a highlights the correspondance between the measured velocity profile and the magnetic field structure in this region: the acceleration takes place orthogonal to the angle of the magnetic separatrix of the last cusp. In the investigated region the ions reach a maximum axial velocity of 14800 m/s. The combination of the axial and 30° velocity components (v_{ax} and v_{30}, respectively) permits calculation of the radial ion velocity component (v_r) at each point, plotted in Fig. 5c:

$$\tan(\theta) = \frac{1}{\tan(30°)} - \frac{v_{30}}{v_{ax}\sin(30°)} \tag{7}$$

$$v_r = v_{ax}\tan(\theta) \tag{8}$$

where θ is the total velocity vector angle from the thruster axis. The radial velocities follow the same general pattern as the axial components, starting at low values in the thruster discharge channel and increasing in magnitude after the acceleration zone along the magnetic separatrix. As required for efficient conversion of ion momentum to thrust, the axial velocity components are greater in magnitude than the radial components.

The total calculated velocity vectors are shown in Fig. 5d. Note that for slow velocities, the calculated angle θ is very sensitive to small variations in the measured values; thus, angles calculated to be slightly negative are shown forced to zero for a physical result. The ions slowly move downstream inside the discharge channel until they are sharply accelerated in the vicinity of the last magnetic cusp at a mean angle of 31.2°, roughly orthogonal to the first magnetic field line to bend out of the channel. The maximum measured velocity of 19300 m/s occurs at the point ($R = 8$ mm, $Z = 2$ mm). Previous plasma potential measurements in this region[12] obtained with a floating emissive probe, reproduced in Fig. 5e, show consistency with the measured velocity profile. Equipotential lines indicate about a 180 V potential drop through the separatrix, leading to a theoretical increase in xenon ion velocity of $\Delta v = \sqrt{2q\Delta\phi/M_i} = 16255$ m/s – which is in good agreement with the measured velocity values. We note that by adjusting the measured potential 2 mm in

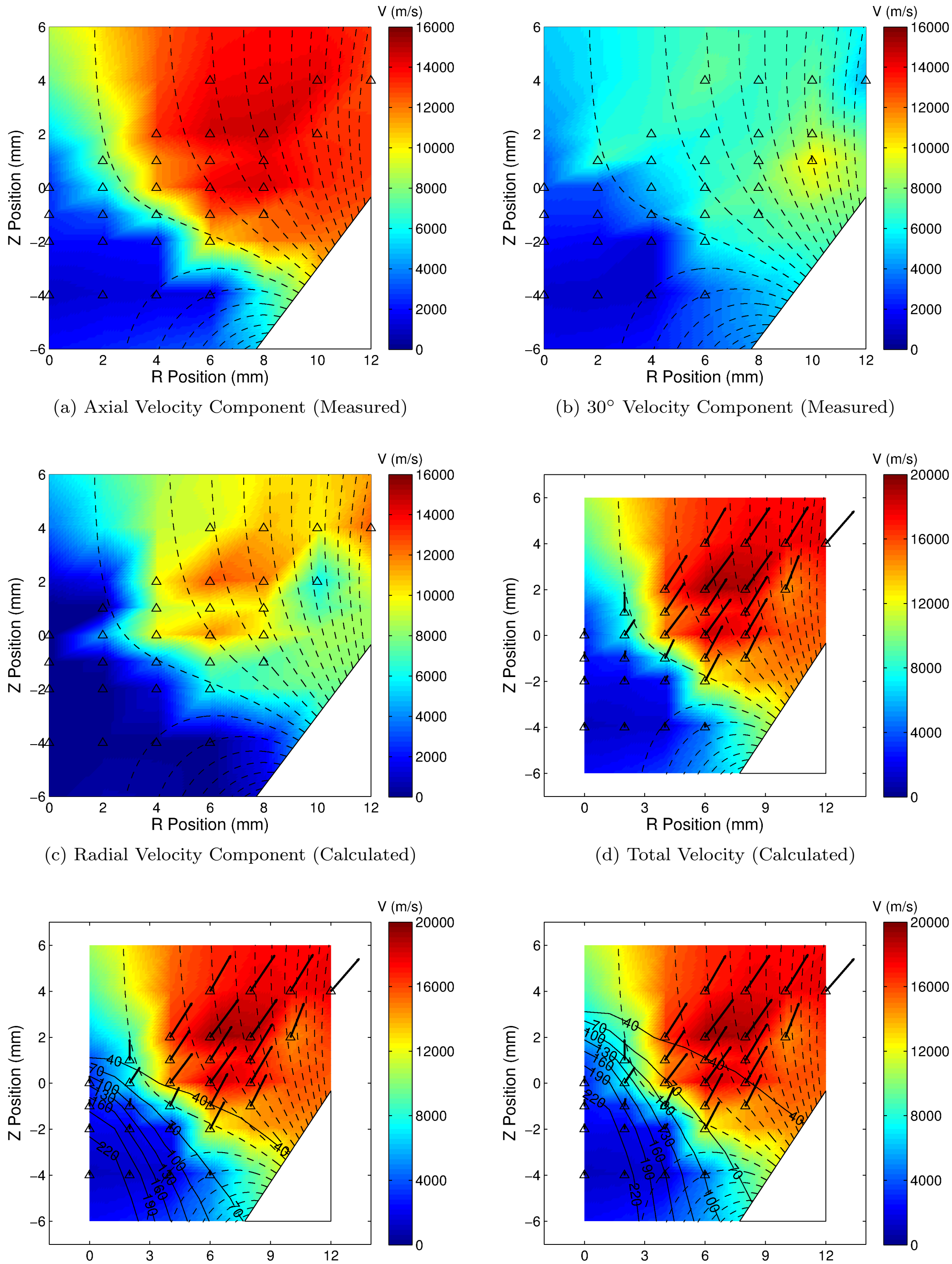

(a) Axial Velocity Component (Measured)

(b) 30° Velocity Component (Measured)

(c) Radial Velocity Component (Calculated)

(d) Total Velocity (Calculated)

(e) Total Velocity with Measured Potential

(f) Total Velocity with Adjustusted Potential

Figure 5: Compiled LIF data for the CCFT operating at 300 V anode potential and 586 μg/s xenon mass flow rate. The external cathode is located at $R = 30$ mm and $Z = 28.3$ mm, oriented in the $-R$ direction. Calculated (dotted) magnetic field lines from FEMM[13] are indicated. LIF scans are taken with the exciting beam (a) parallel to the main axis ($R = 0$) and (b) 30° from $R = 0$ in a CCW rotation. The two data sets permit calculation of the (c) radial velocity components and (d) total velocity vector magnitudes and directions. Previously measured potential data are superimposed in (e). Adjusting the measured potential 2 mm in the $+Z$ direction in (f) illustrates how ions are most likely accelerated by the steep potential drop in directions orthogonal to the equipotential lines.

the $+Z$ direction (Fig. 5f), we achieve an even more physically consistent picture where accelerated ions are traveling nearly orthogonal to the 40 V equipotential line by the end of the potential drop. This small shift in position could be accounted for with uncertainties in probe position and LIF system alignment between the two distinct experiments, as well as the intrusive nature of the emissive probe that could push a measured potential drop upstream.

Note that for $Z \geq 4$ near the centerline, the signal-to-noise ratio (SNR) substantially drops and the determination of a reliable peak in the fluorescence signal is more difficult. This low SNR region continues while moving downstream for radii less than that of the high velocity conical region. A possible explanation is the lower ion density here in comparison with the high velocity region (which emits strong visible radiation, see Fig. 1b). This feature has been identified in previous Faraday probe measurements[20] which show two large peaks in the collected ion current density at angles corresponding to the high velocity conical plume.

These experimental measurements highlight how the ion velocity field, the magnetic field and the the electrostatic potential field are all correlated. Magnetized electrons, influenced by the magnetic cusp geometry, set up the electrostatic field that in turn sets the acceleration regions and shapes the final ion trajectories. Since the ions are unmagnetized (with Larmor radii much larger than the thruster dimensions), the ion motion may be considered to be indirectly determined by the magnetic field topology. In the next section we investigate these relationships further through a numerical approach.

IV. 3D Particle-In-Cell Simulations

The CCFT has been simulated with the 3D Particle-In-Cell (PIC) code F3MPIC,[14] developed at the University of Padova, to provide additional insight into the particle dynamics inside the discharge channel and emitted plume. Particular focus is given to the region near the last magnetic separatrix where strong ionization and acceleration regions are experimentally observed. Various PIC codes have been previously used to successfully model plasma propulsion systems like the CCFT.[16–18]

A. Code Overview

In F3MPIC, the classical PIC algorithm is coupled with a 3D finite element electrostatic and electromagnetic solver in time. The code is built on an unstructured mesh of tetrahedra, allowing for arbitrary geometries, and the PIC core is comprised of a Boris-Leapfrog scheme that can manage multiple species, both charged and neutral. A magnetic field with an arbitrary topology can be imposed to study magnetized particle dynamics. Particles are tracked inside the tetrahedra using a fast priority-sorting algorithm. Electromagnetic interactions between charged particles are treated self-consistently. At each time step, charge density and plasma current density arising from the particle motion are calculated and weighted on the nodes of the mesh.

The electrostatic and the electromagnetic fields are then computed by solving Poisson's equation or the full set of Maxwell's equations including both plasma source terms (charge density and plasma currents) and external source terms (e.g. a polarized electrode or the current flowing through an antenna). The solver employs a finite element method. The electrostic field can be solved in either 2D axisymmetry or full 3D. Both plasma and non-plasma regions (e.g. vacuum, conducting elements) may be incorporated. A Monte-Carlo module is included to take account of neutral-charged particle collisions, described by the proper cross-sections for the chemical species involved. Different types of surfaces have been implemented: conductors, dielectrics, exit ports, neutral emitters, and charged particle emitters. Spatial distributions of plasma properties, electric and magnetic fields can be recorded at desired time steps. Control surfaces can be arbitrarily defined in the simulation domain to record the positions and velocities of passing particles, allowing distribution functions, mass flow rates, thrusts and beam divergence angles to be computed.

B. Cylindrical Cusped Field Thruster Simulation

The geometry of the CCFT, including the external cathode, has been mapped to a tetrahedral mesh by the 3D finite element grid generator GMSH (see Fig. 6). The simulation domain is comprised of two main cylindrical regions: the thruster discharge channel and the vacuum ejection volume. The former is 14 mm in diameter and 36 mm long, while the latter is 40 mm in diameter and 84 mm long. The cathode is modeled as a cylindrical cavity in the ejection volume located 35 mm downstream of the thruster exit plane. The mesh size Δx is chosen in each simulation to satisfy the condition $\Delta x < \lambda_{De}$, the Debye length. Differently sized tetrahedra are used throughout the domain: the mesh is denser in the thruster channel to account for higher plasma density and is coarser in the expansion volume. The mesh consists of about 332,000 tetrahedra.

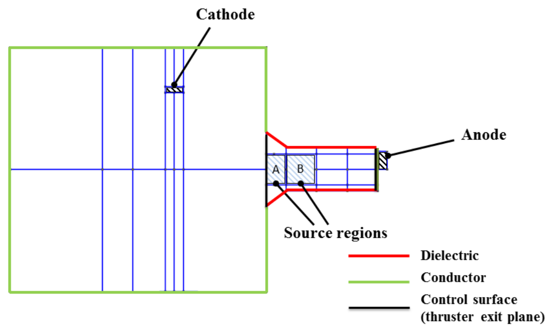

(a)

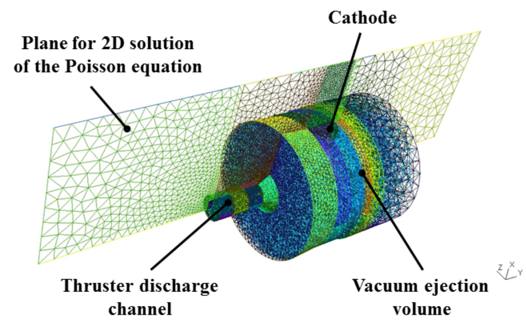

(b)

Figure 6: (a) Simulated thruster geometry with electron emitting cathode, electron and ion emitting ionization source regions, and electron absorbing anode indicated. (b) Generated 3D tetrahedral mesh over the computational domain with the 2D Poisson solution plane superimposed.

The simulated magnetostatic field topology reproduces the two cusps located inside the discharge channel and the magnetic separatrix at the diverging channel exit (see Fig. 1a). We simulate a fully ionized collisionless plasma comprised of electrons and singly charged xenon ions. Both ions and electrons are treated kinetically with a simulation time step set to resolve the fastest characteristic plasma period (in this case the electron cyclotron period). A detailed model of the ionization mechanism is neglected here; rather, the effect of ionization is represented by loading a certain number of both ions and electrons in defined source regions (A and B) at each time step (see Fig. 6a). The source rates in region A and B are 1×10^{12} particles/s and 0.5×10^{12} particles/s, respectively. A higher source rate is used close to the exit plane near the final cusp where we expect strong ionization and previous measurements indicate a steep potential drop.[12]

The electrons and ions are generated according to a Maxwellian distribution with temperatures of 1.3 eV and 0.1 eV, respectively. The cathode is represented by an electron emitting surface that ejects 25 eV particles according to the applied experimental keeper potential. The discharge channel walls are represented as dielectrics that specularly reflect incident particles, while the plasma ejection volume boundary and anode are defined as conductors that remove incident particles from the simulation domain. Note that the F3MPIC conductor boundary condition applies to particles reaching the physical device walls only and does not influence the electrostatic field solver, whose constraints are defined separately.

Although the code can compute electrostatic fields in 3D, these simulations solve the Poisson equation on a 2D (radial-axial) plane (pictured in Fig. 6b) to reduce computation time. The cathode and anode appear as polarized rectangular surfaces on this 2D longitudinal plane. The fields are then applied at the nodes of the 3D mesh through an axisymmetric (azimuthal) revolution of the plane. Note that in physical space, the cathode and anode boundaries are not revolved in this manner and are located as in the real device. To represent the experimental operation conditions of Sec. III.B with 300 V anode potential and ~ 25 V plasma potential near the cathode, the simulated anode is given 275 V and the simulated cathode is given 0 V.

An issue originates from the significantly different ion and the electron time scales. Due to the high magnetic field intensity in the cusps (0.45 T), the minimum electron cyclotron period is relatively fast (about 8×10^{-11} s), requiring a time step of at least 4×10^{-11} s. The ions need on order of a few microseconds to exit the discharge channel and fill the ejection volume. The required number of time steps is then 2.5×10^5, leading to an impractically long run time for the simulations. To address this issue, simulations are advanced for about 10 μs with a rough time step (10^{-9} s), followed by an additional 1.5 μs with a refined time step of 4×10^{-11} s.

The number of computational particles in the domain is continously monitored to determine when a steady condition is reached; at each time step we verify that the number of particles exiting the domain is balanced by the number of particles loaded. The simulations presented here comprise about 1.2×10^7 particles. In the thruster discharge channel, the steady state plasma density is about 4×10^{15} m^{-3}. Simulations with higher densities imply either a greater number of simulated macroparticles, increasing the computation time, or a higher weight per particle which can increase the numerical noise. Moreover, higher densities require a denser mesh to satisfy the Debye length restriction. Thus, we accept a lower simulated density than observed in the real thruster to limit the computational effort.

We record the position and velocity of the particles crossing the exit plane at each time step. Post-processing tools are then used to estimate mass flow rates, currents and velocity distribution functions in the thruster plume. Figures 7 and 8 illustrate the ion and electron densities at different times throughout the simulation. We observe an initial outward flow of electrons from the discharge channel, followed by the slower ions. The latter take about 2 μs to begin leaving the channel and 5 μs to reach the opposite boundary of the ejection volume.

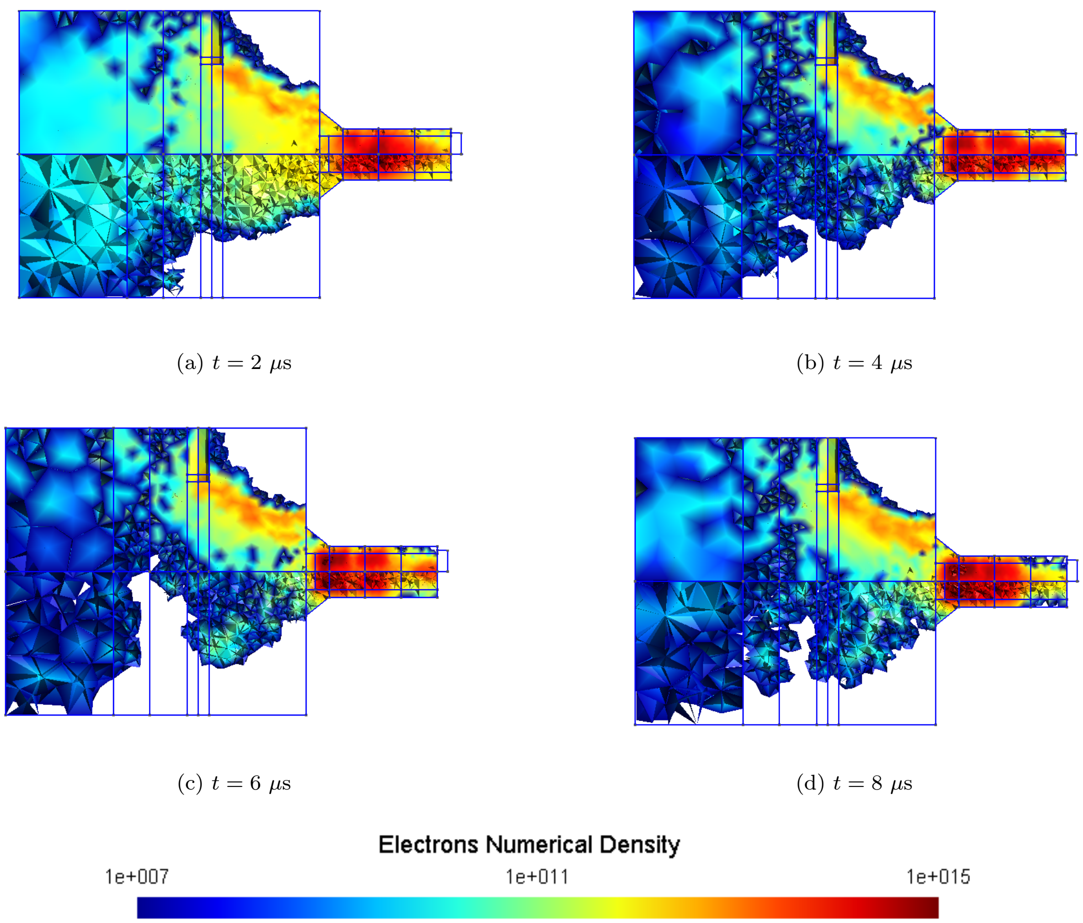

(a) $t = 2\ \mu$s

(b) $t = 4\ \mu$s

(c) $t = 6\ \mu$s

(d) $t = 8\ \mu$s

Figure 7: Computed electron density profiles (in m^{-3}) at various time steps.

Apparent in both the electron and ion density plots is the presence of a higher density conical region with a divergence angle between $25° - 30°$ relative to the thruster axis, originating near the exit plane. A cross section taken about 2 cm into the plume in Fig. 9 confirms the thin annular area of elevated ion density. This feature is characteristic of the cusped field thrusters and can be visually observed during thruster operation. The simulated divergence angle of the plume is in agreement with the experimentally determined mean ion velocity vector angle of 31° and the visible plume in Fig. 1b. A similar value can also be derived from Faraday probe measurements of the CCFT operating on krypton.[20]

The electrons emitted by the cathode are mainly guided by the magnetic field lines towards the cusp near the exit plane. In the discharge channel, electrons are strongly magnetized and become trapped by the magnetic cusps; higher electron density is thus observed in these regions, which is readily apparent in Fig. 10 where the magnetic field lines have been superimposed. The magnetic field confines electrons in the

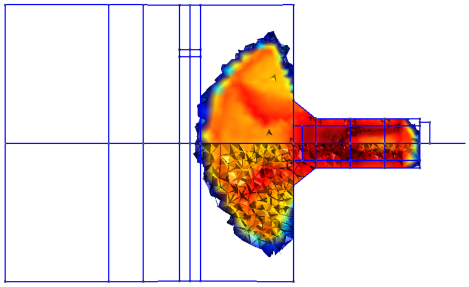

(a) $t = 2$ μs

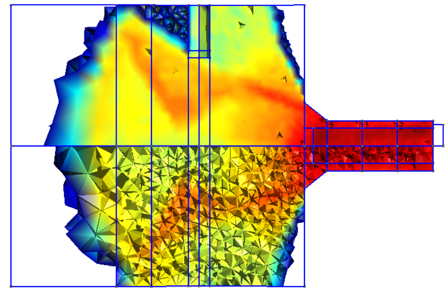

(b) $t = 4$ μs

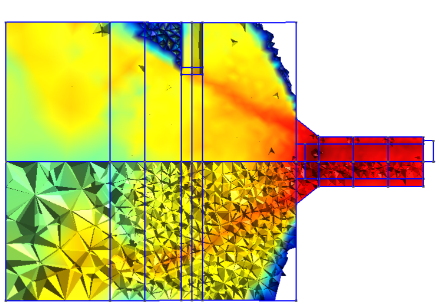

(c) $t = 6$ μs

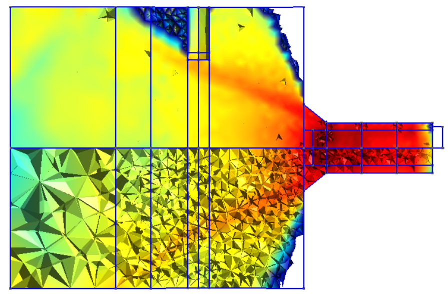

(d) $t = 8$ μs

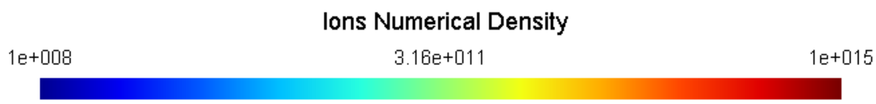

Figure 8: Computed ion density profiles (in m^{-3}) at various time steps. The ions lag the electrons leaving the thruster discharge channel.

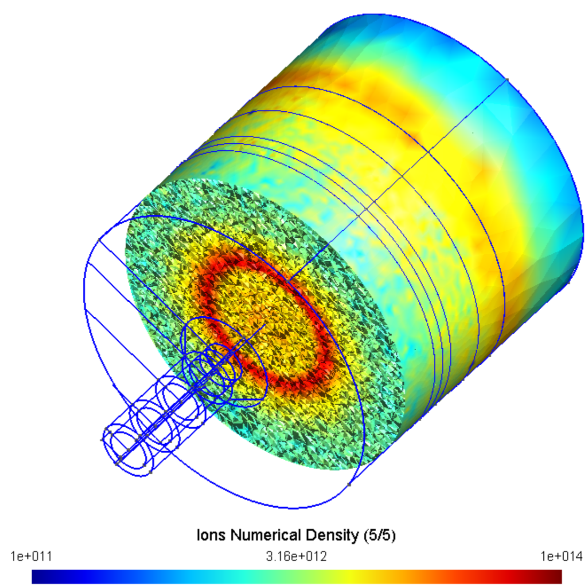

Figure 9: Cross section of the plume ion density distribution (in m^{-3}) highlighting the presence of a higher density annular region.

central region of the discharge channel, with the exception of the cusps. In contrast, ion density is higher in the region between cusps where the field lines are parallel to the wall (Fig. 11).

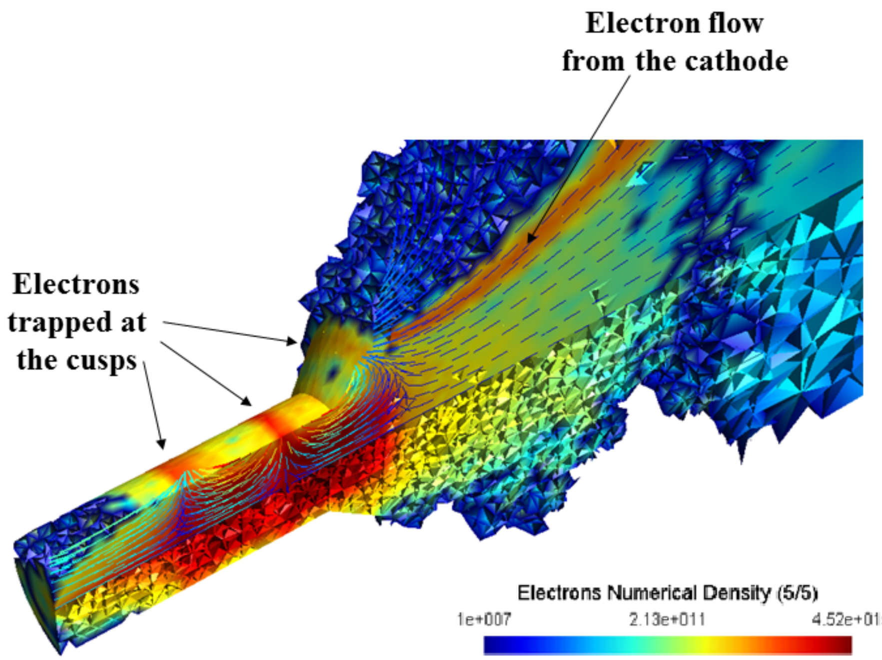

Figure 10: Electron density (in m^{-3}) in the discharge channel with magnetic field lines superimposed illustrating electrons collecting near the cusps.

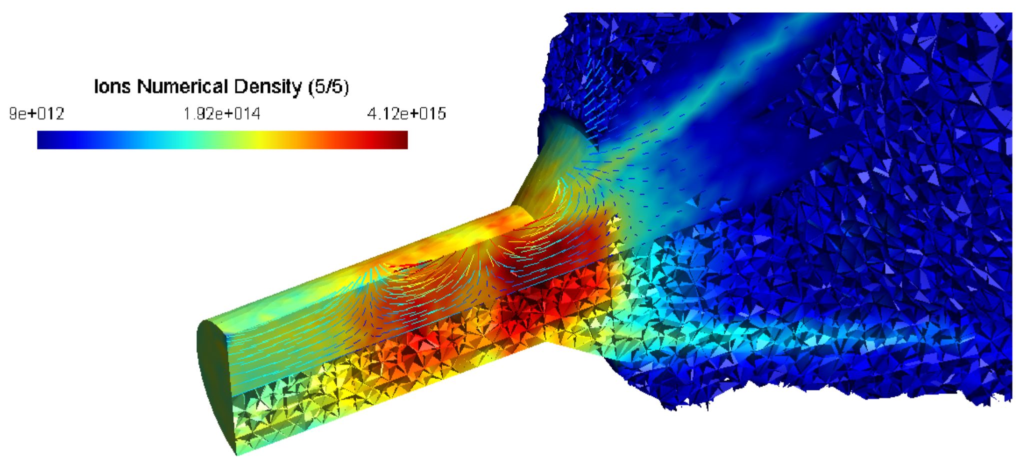

Figure 11: Ion density (in m^{-3}) in the discharge channel with magnetic field lines superimposed.

The calculated electrostatic potential is presented in Fig. 12. The view in Fig. 12a shows a strong potential drop located near the thruster exit plane which strongly accelerates ions downstream. This feature has also been observed experimentally with a floating emissive probe,[12] where potential changes of >180 V occur within a few millimeters. In contrast, the simulated potential drop takes place over a few centimeters. A possible reason for this discrepancy is the lower plasma density present in the simulation in comparison with the real system. The spatial scale of the potential drop (and sheath thickness) can be considered proportional to the Debye length, which increases as density decreases.

The positions and velocities of particles crossing the exit plane have been recorded during the last 5×10^{-8} s of the simulation in order to determine the radial velocity distributions. The collected axial and radial ion

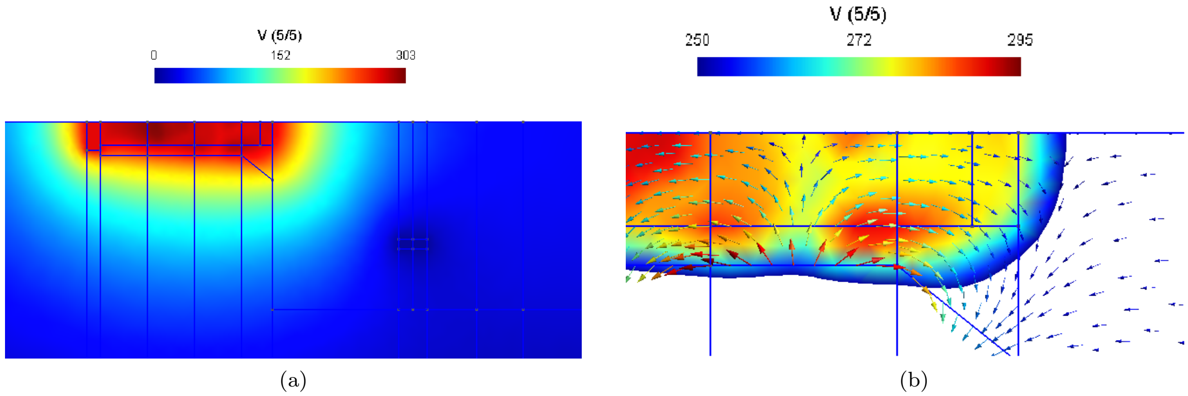

Figure 12: (a) Simulated potential distribution (in V) in the thruster discharge channel with (b) a detailed view of the thruster exit plane region with magnetic flux vectors superimposed.

velocity components as a function of radius are plotted in Fig. 13. The axial component is characterized by two different populations: a low velocity population present throughout the plane and a high velocity population located at radii greater than 8 mm, which is apparent in the ion velocity distribution functions (IVDFs) shown at two radial positions in Fig. 13c. At $R = 2$ mm a dense low velocity population and a sparse higher velocity population are observed. In contrast, by $R = 10$ mm the predominant population has been accelerated to 12000 m/s and a sparse low velocity population persists near 4500 m/s. The simulated IVDFs qualitatively agree with the LIF velocity measurements performed here, which show strong ion acceleration in the outer part of the channel and observed velocities up to 14000 m/s. Finally, Fig. 13d illustrates the calculated ion current density at the exit plane as a function of radius. The profile exhibits the high density wings of the divergent thruster plume discussed above.

The fully kinetic 3D PIC simulations reproduce several characteristics of the CCFT discharge observed experimentally. The code proves to be an effective tool for investigating thruster behavior and supporting the interpretation of the experimental measurements. Finally, work with F3MPIC is ongoing to help optimize thruster performance, with particular emphasis on shaping the magnetic field structure to increase axial ion velocities and reduce divergence losses in the plume.

V. Conclusion

This work aims to provide new insight into the physical mechanisms occuring in the discharge channel and ejection region of the Stanford Cylindrical Cusped Field Thruster through a combined experimental and computational approach. Xenon laser induced fluorescence measurements have determined total ion velocities (both magnitude and direction) at several points near the thruster exit plane that are consistent with previous electrostatic potential measurements. The thruster has also been simulated using the particle-in-cell code F3MPIC developed at the University of Padova. Agreement between simulation and experimental results highlights the capability of the code to reproduce several physical features of the thruster.

We show that the electrons are strongly magnetized and that their density distribution coincides with the cusped magnetic field structure. Ion acceleration is localized in a narrow region close the thruster exit plane where a strong potential drop occurs. The acceleration front follows the magnetic separatrix and directs ions on a divergent trajectory into the plume with observed increases in ion density at the outer radii of the exit plane. We believe that the magnetic field topology, which directly shapes the spatial electron density distribution and the electrostatic potential structure, indirectly affects ion dynamics in this region through the creation of ionization and acceleration zones. The plasma plume is characterized by a dense conical layer with a 30° half angle. Work is ongoing at the SPPL to improve spatial resolution of the LIF ion velocity measurement and obtain full ion velocity distribution functions at each measurement location. Further analysis with the F3MPIC code will explore the effects of altering the magnetic field structure to reduce plume divergence.

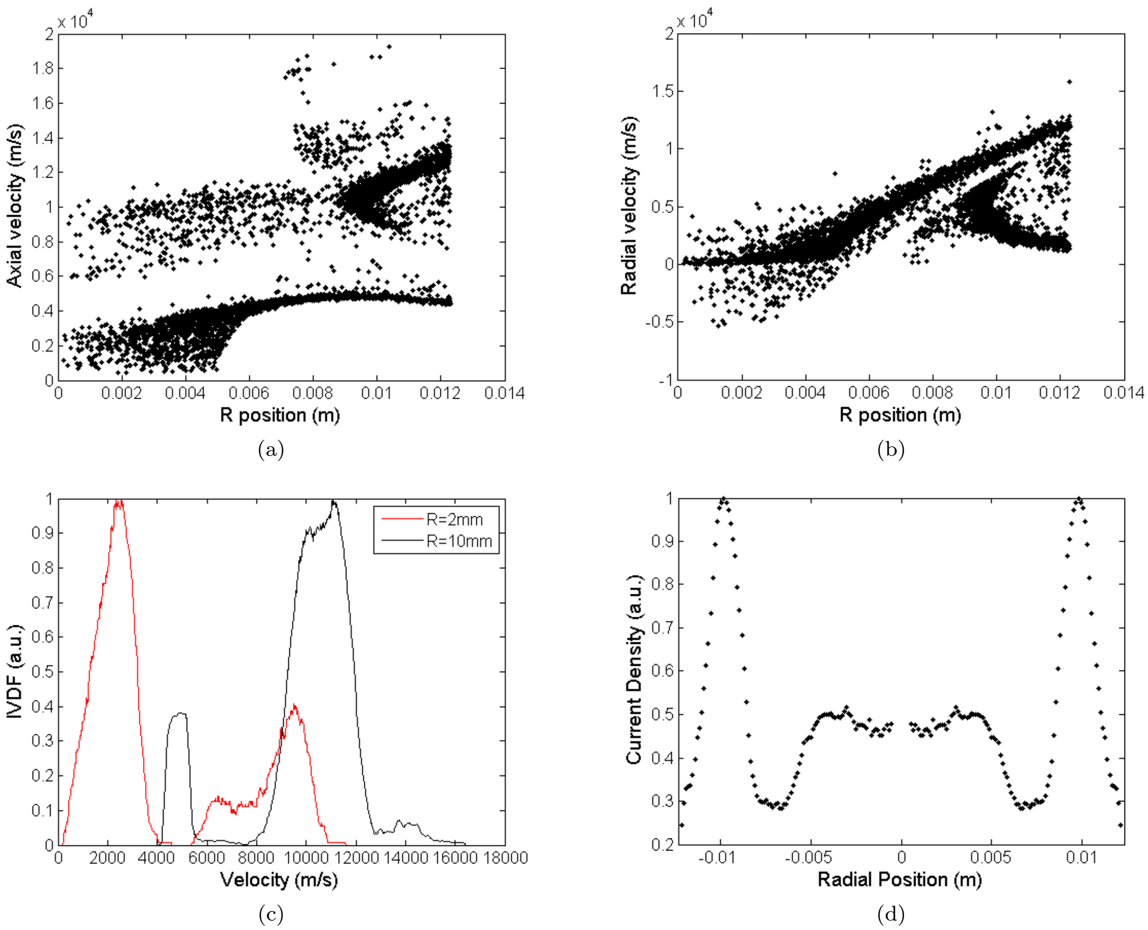

Figure 13: (a) Axial and (b) radial velocity components of ions crossing the exit plane as a function of radius. (c) Calculated ion velocity distribution functions at the exit plane for two radial positions, 2 mm and 10 mm. (d) Calculated ion current density at the exit plane as a function of radius demonstrating the high density wings observed in the plume.

Acknowledgments

F3MPIC has been developed under the HPH.com project funded by the EU FP7 (Grant Number 218862). The authors thank D. Rondini and D. Curreli for essential contributions to code development. ALF thanks the "Fondazione Aldo Gini" scholarship for supporting his 2012 period at Stanford University. The authors acknowledge support from the Air Force Office of Scientific Research. CVY acknowledges support from the DOE NNSA Stewardship Science Graduate Fellowship under contract DE-FC52-08NA28752.

References

[1]Khayms, V. and Martinez-Sanchez, M., "Design of a Miniaturized Hall Thruster for Microsatellites," *Proceedings of the 32nd AIAA/ASME/SAE/ASEE, Joint Propulsion Conference & Exhibit, Lake Buena Vista, FL*, July 1996, AIAA Paper 96-3291.

[2]Schmidt, D. P., Meezan, N. B., Hargus Jr, W. A., and Cappelli, M. A., "A Low-Power, Linear-Geometry Hall Plasma Source with an Open Electron-Drift," *Plasma Sources Science and Technology*, Vol. 9, 2000, pp. 68–76.

[3]Kim, V., "Main Physical Features and Processes Determining the Performance of Stationary Plasma Thrusters," *Journal of Propulsion and Power*, Vol. 14, No. 5, 1998, pp. 736–743.

[4]Raitses, Y. and Fisch, N. J., "Parametric Investigations of a Nonconventional Hall Thruster," *Physics of Plasmas*, Vol. 8, No. 5, 2001, pp. 2579–2586.

[5]Courtney, D. G. and Martinez-Sanchez, M., "Diverging Cusped-Field Hall Thruster (DCHT)," *Proceedings of the 30th International Electric Propulsion Conference, Florence, Italy*, September 2007, IEPC-2007-039.

[6]Young, C. V., Smith, A. W., and Cappelli, M. A., "Preliminary Characterization of a Diverging Cusped Field (DCF) Thruster," *Proceedings of the 31st International Electric Propulsion Conference, Ann Arbor, MI*, September 2009, IEPC-2009-166.

[7]Raitses, Y., Granstedt, E., Smirnov, A., Merino, E., and Fisch, N. J., "Effects of Cathode Electron Emission on Hall Thruster Discharge," *Proceedings of the 44th AIAA/ASME/SAE/ASEE Joint Propulsion Conference & Exhibit, Hartford, CT*, July 2008, AIAA Paper 2008-5188.

[8]Raitses, Y., Smirnov, A., and Fisch, N. J., "Cylindrical Hall Thrusters," *Proceedings of the 37th AIAA Plasmadynamics and Lasers Conference, San Francisco, CA*, June 2006, AIAA Paper 2006-3245.

[9]Smirnov, A., Raitses, Y., and Fisch, N. J., "Plasma Measurements in a 100 W Cylindrical Hall Thruster," *Journal of Applied Physics*, Vol. 95, No. 5, 2004, pp. 2283–2292.

[10]Smirnov, A., Raitses, Y., and Fisch, N. J., "Experimental and Theoretical Studies of Cylindrical Hall Thrusters," *Physics of Plasmas*, Vol. 14, 2007, pp. 057106.

[11]Courtney, D. G., Lozano, P., and Martinez-Sanchez, M., "Continued Investigation of Diverging Cusped Field Thruster," *Proceedings of the 44th AIAA/ASME/SAE/ASEE Joint Propulsion Conference & Exhibit, Hartford, CT*, July 2008, AIAA Paper 2008-4631.

[12]MacDonald, N. A., Young, C. V., Cappelli, M. A., and Hargus Jr, W. A., "Ion Velocity and Plasma Potential Measurements of a Cylindrical Cusped Field Thruster," *Journal of Applied Physics*, Vol. 111, No. 9, 2012, pp. 093303.

[13]Meeker, D., "Finite Element Method Magnetics," www.femm.info, Jun 2011.

[14]Pavarin, D., Ferri, F., Manente, M., Curreli, D., Melazzi, D., Rondini, D., and Cardinali, A., "Development of Plasma Codes for the Design of Mini-Helicon Thrusters," *Proceedings of 32nd International Electric Propulsion Conference, Wiesbaden, Germany*, September 2011, IEPC-2011-240.

[15]Verboncoeur, J., "Particle Simulation of Plasmas: Review and Advances," *Plasma Physics and Control Fusion*, Vol. 47, 2006, pp. A231–A260.

[16]Fife, J. and Martinez-Sanchez, M., "Two-Dimensional Hybrid Particle-In-Cell (PIC) Modeling of Hall Thrusters," *Proceedings of 24th International Electric Propulsion Conference, Moscow, Russia*, September 1995, IEPC-95-240.

[17]VanGilder, D., Font, G., and Boyd, I., "Hybrid Monte Carlo Particle-in-Cell Simulation of an Ion Thruster Plume," *Journal of Propulsion and Power*, Vol. 15, No. 4, 1999, pp. 530–538.

[18]Gildea, S. R., *Development of the Plasma Thruster Particle-in-Cell Simulator to Complement Empirical Studies of a Low-Power Cusped-Field Thruster*, Ph.D. thesis, Massachusetts Institute of Technology, Oct 2012.

[19]Manzolaro, M., Manente, M., Curreli, D., Vasquez, J., Montano, J., Andrighetto, A., Scarpa, D., Meneghetti, G., and Pavarin, D., "Off-Line Ionization Tests Using the Surface and the Plasma Ion Sources of the SPES Project," *Review of Scientific Instruments*, Vol. 83, No. 2, 2012, pp. 02A907.

[20]Young, C. V., "The Stanford Diverging Cusped Field Thruster: Design, Construction, and Initial Testing," Undergraduate Honors Thesis, Stanford University, Jun 2010.

[21]MacDonald, N. A., *Laser Induced Fluorescence Characterization of Cusped Field Plasma Thrusters*, Ph.D. thesis, Stanford University, June 2012.

[22]Mazouffre, S., Gawron, D., and Sadeghi, N., "A Time-Resolved Laser Induced Fluorescence Study on the Ion Velocity Distribution Function in a Hall Thruster After a Fast Current Disruption," *Physics of Plasmas*, Vol. 16, No. 4, 2009, pp. 043504.

[23]Hargus Jr, W. A. and Charles, C. S., "Near-Plume Laser-Induced Fluorescence Velocity Measurements of a Medium Power Hall Thruster," *Journal of Propulsion and Power*, Vol. 26, No. 1, 2010, pp. 135–141.

[24]Gawron, D., Mazouffre, S., Sadeghi, N., and Heron, A., "Influence of Magnetic Field and Discharge Voltage on the Acceleration Layer Features in a Hall Effect Thruster," *Plasma Sources Science and Technology*, Vol. 17, No. 2, 2008, pp. 025001.

[25]MacDonald, N. A., Cappelli, M. A., Gildea, S. R., Martinez-Sanchez, M., and Hargus Jr, W. A., "Laser-Induced Fluorescence Velocity Measurements of a Diverging Cusped-Field Thruster," *Journal of Physics D: Applied Physics*, Vol. 44, No. 29, 2011, pp. 295203.